Micromechanic Modeling and Analysis of the Flow Regimes in Horizontal Pneumatic Conveying

S. B. Kuang and A. B. Yu
Laboratory for Simulation and Modelling of Particulate Systems, School of Materials Science and Engineering,
The University of New South Wales, Sydney, NSW 2052, Australia

DOI 10.1002/aic.12480

Pneumatic conveying is an important technology for industries to transport bulk materials from one location to another. Different flow regimes have been observed in such transportation processes, but the underlying fundamentals are not clear. This article presents a three-dimensional (3-D) numerical study of horizontal pneumatic conveying by a combined approach of discrete element model for particles and computational fluid dynamics for gas. This particle scale, micromechanic approach is verified by comparing the calculated and measured results in terms of particle flow pattern and gas pressure drop. It is shown that flow regimes usually encountered in horizontal pneumatic conveying, including slug flow, stratified flow, dispersed flow and transition flow between slug flow and stratified flow, and the corresponding phase diagram can be reproduced. The forces governing the behavior of particles, such as the particle–particle, particle-fluid and particle-wall forces, are then analyzed in detail. It is shown that the roles of these forces vary with flow regimes. A general phase diagram in terms of these forces is proposed to describe the flow regimes in horizontal pneumatic conveying. *AIChE J,* 57: 2708–2725, 2011
Keywords: pneumatic conveying, flow regime, phase diagram, discrete element method, computational fluid dynamics

Introduction

Pneumatic conveying has many industrial applications and generally involves two flow regimes: dense-phase flow and dilute-phase flow.[1] The dense-phase flow conveys particles in terms of slug flow or moving bed, with power consumption and product damage lower than those of dilute-phase flow. The dilute-phase flow where particles are dispersed throughout an entire pipe is, however, suited for a wider range of materials. Therefore, flow regimes are of great importance to pneumatic conveying, particularly for horizontal pipelines, where particles exhibit more complicated behaviors compared to those in vertical pipelines due to their gravity perpendicular to the conveying direction. The flow regimes in horizontal pneumatic conveying typically include slug flow, stratified flow, dispersed flow, and transition flow between slug flow and stratified flow.[2,3]

Previous studies have shown that many variables affect flow regimes, including materials properties, operating conditions, and system geometries. Based on the studies of these variables, some general knowledge about flow regimes has been obtained. For example, materials and bulk properties, such as particle size and density, bulk density, permeability, air retention and deaeration, can be used to predict flow regimes,[4,5] and the characteristics of pressure fluctuation have a good capability for online identification of flow

---

Correspondence concerning this article should be addressed to A. B. Yu at a.yu@unsw.edu.au.

regimes.[6–10] In addition, a transition flow zone is identified between the slug-flow regime and the stratified flow, where conveying pipelines are very vulnerable to blockage.[11–14] Some semi theoretical correlations have also been formulated to predict the pressure drop in different flow regimes,[14,15] and the boundaries between flow regimes.[11,16–18] These results are useful in solving some practical problems. However, to date, the mechanisms underlying flow regimes identified and their transition are not clearly understood. The applications of pneumatic conveying largely depend on empirical experience, as recently pointed out by Park and Klingzing.[6]

Flow regime is a bulk behavior resulting from the collective interactions between particles, particles and wall, particles and fluid. Therefore, analysis of the interaction forces in conjunction with the flow behavior of individual particles can help understand the underlying mechanisms. With advances in measuring techniques for particle-fluid systems in the last two decades,[19,20] the internal structure of flow regimes constructed according to particles position, and the velocities of particle patterns can now be obtained using tomography techniques.[21–24] Particle-wall force is also accessible through the stress transistors.[25–28] However, at this stage of development, little is known about the velocities of individual particles in the dense-phase conveying and in particular, the particle–particle and particle-fluid interaction forces. In principle, computer modeling and simulation can overcome this problem.

Numerical models for particle-fluid systems may be continuum- or discrete-based with respect to the solid phase, as recently reviewed by different investigators.[29–31] The former is typically represented by the so-called two-fluid model (TFM), where particle-phase stresses are described empirically or based on the kinetic theory.[32] TFM is computationally convenient, and, thus, has many applications in pneumatic conveying.[33–41] However, all these applications thus far reported focused on one or two-flow regimes. This may be due to the fact that the effective use of TFM heavily depends on the constitutive or closure relation for the particle-phase stresses, which are not generally available at this stage of development. The discrete approach can be done by the Lagragian particle tracking (LPT), or the combined approach of computational fluid dynamics and discrete element method (CFD-DEM).[42,43] LPT is valid for gas–solid flows where the solid concentration is low and, hence, particle–particle interaction is not important.[44–47] On the contrary, CFD-DEM has no such limitations and is, thus, applicable to a wide range of flow conditions.[30,48]

With this realization, CFD-DEM has been increasingly used to study pneumatic conveying in various aspects, including flow regimes, as recently summarized by Kuang et al.[49] These studies can improve the understanding of pneumatic conveying. However, to date, most of these studies were based on simplified models where 3-D particle flow was sometimes treated as 2-D, and gas flow was 2-D or 1-D. In 2-D DEM simulations, particles lose their motion in the third dimension and the fluid-drag force has to be based on unrealistic porosity. On the other hand, 1-D CFD misses the radial pressure and flow characteristics. As a result, some key flow features in pneumatic conveying are missing in the previous studies, particularly in the studies of flow regimes. For example, Lim et al.[50] could only obtain the slug flow and dispersed flow in their 2-D CFD-DEM model; the stratified flow and the transition flow were missing. Fraige and Langston[51] demonstrated their 1-D CFD-3-D DEM model could produce the slug flow, stratified flow, and dispersed flow in horizontal pneumatic conveying. However, the three flow regimes were obtained by changing particle rotation rather than gas-flow velocity as observed in experiments. Moreover, the transitional flow which is often associated with long slugs in horizontal conveying was not obtained in all the previous numerical studies. To overcome this problem, a 3-D CFD-DEM model is necessary. In recent years, some efforts have been made in this direction. For example, Strauß et al[52,53] developed a 3-D CFD-DEM for horizontal and vertical slug flow, where gas flow was described by the Darcy law to avoid CFD effort. Chu and Yu[54] integrated a 3-D DEM model into the commercial CFD package Fluent for the study of gas–solid flow through a bend. Kuang et al[55] developed a 3-D CFD-DEM model to study flow phenomena in pneumatic conveying. The model has been applied to the study of flow regimes in vertical pneumatic conveying.[49] However, to date, comprehensive 3-D CFD-DEM modeling and analysis of the flow regimes in horizontal pneumatic conveying have not been found in the literature.

In this work, the 3-D CFD-DEM model of Kuang et al.[49] for vertical pneumatic conveying are extended to study the flow regimes in horizontal pneumatic conveying. The article is organized as follows. The numerical model is first introduced and a typical flow condition as a base case is studied focused on the resulting flow patterns and the forces governing the motion of particles. Based on this analysis, a new phase diagram in terms of these forces is established. Finally, the generality of this diagram is examined from data obtained under different conditions and corresponding to different flow regimes in horizontal pneumatic conveying.

Simulation Method

The current 3-D CFD-DEM model is that proposed in our previous study of vertical pneumatic conveying, which has been quantitatively validated with respect to key parameters such as slug velocity and gas pressure.[49] For completeness, we only describe the key features of the model later.

Governing equations for particle flow

The solid phase is treated as a discrete phase described by DEM. Hence, the translational and rotational motions of a particle are determined by Newton's second law of motion, i.e.

$$m_i \frac{d\mathbf{v}_i}{dt} = \mathbf{f}_{pgf,i} + \mathbf{f}_{\mathrm{drag},i} + \sum_{j=1}^{k_i} \left(\mathbf{f}_{c,ij} + \mathbf{f}_{d,ij} \right) + m_i \mathbf{g} \tag{1}$$

and

$$I_i \frac{d\boldsymbol{\omega}_i}{dt} = \sum_{j=1}^{k_i} \left(\mathbf{T}_{t,ij} + \mathbf{T}_{r,ij} \right) \tag{2}$$

where m_i, I_i, $\mathbf{v}_i$, and $\boldsymbol{\omega}_i$ are, respectively, the mass, momentum of rotational inertia, translational and rotational velocities of particle i. The forces involved are: (1) the pressure gradient force, given by

Table 1. Components of Forces and Torques Acting on Particle i

Forces and torques		Symbol	Equations
Normal forces	contact	$\mathbf{f}_{cn,ij}$	$-\frac{4}{3}E^*\sqrt{R^*}\delta_n^{3/2}\hat{\mathbf{n}}$
	damping	$\mathbf{f}_{dn,ij}$	$-\gamma_n\left(6m_{ij}E^*\sqrt{R^*\delta_n}\right)^{1/2}\mathbf{v}_{\mathbf{n,ij}}$
Tangential forces	contact	$\mathbf{f}_{ct,ij}$	$-\mu_s\lvert\mathbf{f}_{cn,ij}\rvert[1-(1-\min\{\lvert\delta_{t,ij}\rvert,\delta_{t,ij,\max}\}/\delta_{t,ij,\max})^{3/2}]\hat{\boldsymbol{\delta}}_t$
	damping	$\mathbf{f}_{dt,ij}$	$-\gamma_t\left(6\mu_s m_{ij}\lvert\mathbf{f}_{cn,ij}\rvert\sqrt{1-\delta_{t,ij}/\delta_{t,ij,\max}}\Big/\delta_{t,ij,\max}\right)^{1/2}\mathbf{v}_{t,ij}\ (\delta_{t,ij}<\delta_{t,ij,\max})$
Fluid drag forces		$\mathbf{f}_{drag,i}$	$0.5c_{d0,i}\rho_f\pi R_i^2\varepsilon_{f,i}^2\lvert\mathbf{u}_i-\mathbf{v}_i\rvert(\mathbf{u}_i-\mathbf{v}_i)\varepsilon_{f,i}^{-\chi}$
Pressure gradient force		$\mathbf{f}_{\mathrm{pgf,i}}$	$-\nabla PV_i$
Gravity		$\mathbf{f}_{g,i}$	$m_i\mathbf{g}$
Torque by tangential forces		$\mathbf{T}_{t,ij}$	$\mathbf{R}_{ij}\times(\mathbf{f}_{ct,ij}+\mathbf{f}_{dt,ij})$
Rolling friction torque		$\mathbf{T}_{r,ij}$	$\mu_{r,ij}d_i\lvert\mathbf{f}_{n,ij}\rvert\hat{\boldsymbol{\omega}}_{t,ij}$

where, $\frac{1}{R^*}=\frac{1}{|R_i|}+\frac{1}{|R_j|}$, $E^*=\frac{E}{2(1-v^2)}$, $\hat{\mathbf{n}}=\frac{\mathbf{R}_i}{|\mathbf{R}_i|}$, $\hat{\boldsymbol{\omega}}_{t,ij}=\frac{\boldsymbol{\omega}_{t,ij}}{|\boldsymbol{\omega}_{t,ij}|}$, $\hat{\boldsymbol{\delta}}_t=\frac{\boldsymbol{\delta}_t}{|\boldsymbol{\delta}_t|}$, $\delta_{t,ij,\max}=\mu_s\frac{2-v}{2(1-v)}\delta_n$, $\mathbf{v}_{ij}=\mathbf{v}_j-\mathbf{v}_i+\boldsymbol{\omega}_j\times\mathbf{R}_j-\boldsymbol{\omega}_i\times\mathbf{R}_i$,

$\mathbf{v}_{n,ij}=(\mathbf{v}_{ij}\cdot\hat{\mathbf{n}})\hat{\mathbf{n}}$, $\mathbf{v}_{t,ij}=\mathbf{v}_{ij}-\mathbf{v}_{n,ij}$

$c_{d0,i}=\left(0.63+\frac{4.8}{\mathrm{Re}_{0p,i}^{0.5}}\right)^2$, $\mathrm{Re}_{p,i}=\frac{2\rho_f R_i\varepsilon_{f,i}|\mathbf{u}_i-\mathbf{v}_i|}{\eta_f}$, $\chi=3.7-0.65\exp\left[-\frac{\left(1.5-\log_{10}\mathrm{Re}_{p,i}\right)^2}{2}\right]$

$$\mathbf{f}_{pgf,i}=-\nabla PV_i,$$

where P and V_i are the fluid pressure and the volume of particle i, respectively; (2) the fluid drag force, calculated by

$$\mathbf{f}_{\mathrm{drag},i}=\mathbf{f}_{\mathrm{drag}0,i}\varepsilon_{f,i}^{-\chi}$$

where $\mathbf{f}_{\mathrm{drag}0,i}$, and χ are, respectively, the fluid-drag force on particle i in the absence of other particles and the equation coefficient, and ε_f is the local porosity for the particle; (3) the gravity force $m_i\mathbf{g}$; and (4) the interparticle forces between particles i and j, which include the elastic contact force $\mathbf{f}_{c,ij}$, and the viscous contact damping force $\mathbf{f}_{d,ij}$. The torque acting on particle i by particle j includes two components. One arises from the tangential forces, given by $\mathbf{T}_{t,ij}=\mathbf{R}_{i,j}\times(\mathbf{f}_{ct,ij}+\mathbf{f}_{dt,ij})$, where $\mathbf{R}_{i,j}$ is a vector from the mass center to the contact point; and another is the rolling friction torque given by

$$\mathbf{T}_{r,ij}=\mu_{r,ij}d_i\left|\mathbf{f}_{n,ij}\right|\hat{\boldsymbol{\omega}}_{t,ij},$$

where $\mu_{r,ij}$ is the (dimensionless) rolling friction coefficient, and d_i is particle diameter.[60] The second torque is attributed to the elastic hysteresis loss and viscous dissipation in relation to particle–particle or particle-wall contact, and slows down the relative rotation of particles. For a particle undergoing multiple interactions, the individual interaction forces and torques are summed over the k_i particles in contact with particle i. The interparticle or particle-wall force is calculated according to the nonlinear models commonly used in DEM.[30] For convenience, the equations to calculate these forces are summarized in Table 1.

Note that ε_f is usually calculated over a computational cell. However, the evaluation of ε_f this way is sometimes problematic, particularly for complicated cell configuration. For example, numerical instability may occur because of the rapid temporal and spatial change in porosity and associated properties. This is particularly true for too small CFD cells which may simply have a local porosity fluctuating between zero and unity. To avoid this problem, as used in some of our CFD-DEM studies for complex systems,[49,54,57–59] ϵ_f at a considered point is calculated over a spherical cell. The cell size used in this work is three particle diameters, in connection with our previous study.[58] For a cell close to a wall, its region out of the computational domain should be excluded. All these treatments are consistent with those used in averaging a local macroscopic property.[30]

Governing equations for gas flow

The gas flow is treated as a continuous phase and modeled in a similar way to the one in the conventional two-fluid modeling. Thus, its governing equations are the conservation of mass and momentum in terms of local mean variables over a computational cell, given by

$$\frac{\partial(\rho_f\varepsilon_f)}{\partial t}+\nabla\cdot\left(\rho_f\varepsilon_f\mathbf{u}\right)=0 \tag{3}$$

and

$$\frac{\partial\left(\rho_f\varepsilon_f\mathbf{u}\right)}{\partial t}+\nabla\cdot\left(\rho_f\varepsilon_f\mathbf{u}\mathbf{u}\right)=-\nabla P-\mathbf{F}_{\mathrm{p-f}}+\nabla\cdot\left(\varepsilon_f\boldsymbol{\tau}\right)+\rho_f\varepsilon_f\mathbf{g} \tag{4}$$

where ρ_f, $\mathbf{u}$, P, $\boldsymbol{\tau}$ and $\mathbf{F}_{\mathrm{p\text{-}f}}$ are, respectively, the fluid density, the fluid velocity and pressure, the fluid viscous stress tensor, and the volumetric forces between particles and fluid.

$$\mathbf{F}_{p-f}=\sum_{i=1}^{k_c}\left(\mathbf{f}_{\mathrm{drag},i}+\mathbf{f}_{pgf,i}\right)/\Delta V,$$

where k_c and ΔV are, respectively, the number of particles in a considered computational cell and the volume of the computational cell. $\boldsymbol{\tau}$ is given by is given by an expression analogous to that for a Newtonian fluid. That is

$$\boldsymbol{\tau}=\eta\left[(\nabla\mathbf{u})+(\nabla\mathbf{u})^{-I}\right] \tag{5}$$

Table 2. Flow Conditions Considered in these Simulations

Parameter[a]	Value CASE I[b]	CASE II	CASE III	CASE IV	CASE VI
Pipe diameter, D (m)	0.0563	0.04	0.04	0.05	0.0534
Pipe length, L (m)	7.0	5.0	5.0	0.8	3
Solid flowrate, w (kg/s)	0.533	0.59	0.82	0.34−0.67	0.115−0.46
Gas velocity, U_g (m/s)	9.6−35.0	7.0−40.0	7.0−40.0	1.7−2.3	23.0−35.0
Particle diameter, d_p (m)	0.00318	0.004	0.003	0.003	0.00205
Density, ρ_p (kg/m^3)	1180	1000	1000	1000	2500
Sliding friction coefficient, μ_s	0.5	0.5	0.4	0.3	0.2
Rolling friction coefficient, μ_r	0.04	0.03	0.02	0.01	0.01
Restitution, e	0.8	0.8	0.8	0.9	0.6
Periodic boundary condition in the flow direction	No	No	No	Yes	No
Flow regimes involved[c]	SL, TR, ST, DE	SL, TR, ST, DE	SL, TR, ST, DE	SL	ST

[a] The wall is assumed to have the same properties as particles.
[b] Base case for detailed analysis of flows and forces.
[c] SL is for slug flow regime; TR for transition flow; ST for stratified flow regime; DE for Dispersed flow regime.

It is well established that gas flow is turbulent when its velocity in a pipe is high enough. To describe the turbulent flow, a standard k-ϵ model is employed in the CFD modeling. This helps correctly predict the pressure drop due to the gas-wall friction interaction. Gas turbulence may affect particle flow. However, the studies of circulating fluidized bed and pneumatic conveying systems based on TFM approach manifest that the contribution of gas turbulence to particle flow is negligible.[61–63] This suggestion is tested based on the CFD-DEM simulations in this study. This is done by adding the turbulent dispersion model proposed by Gosman and Ioannides[64] to the DEM to model the effect of gas turbulence on particle flow. The instantaneous fluid velocity other than the mean velocity is used to calculate the fluid-drag force in the CFD-DEM model. The instantaneous velocity consists of the mean velocity obtained by the solution of the time-averaged governing equations of gas phase, and the fluctuating velocity reconstructed from the turbulent kinetic energy according to a Gauss distribution with a zero mean and standard deviation $(2k/3)^{1/2}$. The rest treatments are the same as those used in the CFD-DEM computation. We can, therefore, conduct simulations with or without the turbulent model for gas phase. The results suggest that the inclusion of the turbulent model does not result in any difference in particle behavior under the conditions considered. Therefore, the effect of gas turbulence on particle behavior is not significant for coarse particles, particularly when solid concentration is high. However, further studies are needed to find if this consideration can be applied to fine particles, or generally to gas–solid flow.

Solution and coupling schemes

The method for numerical solution of a CFD-DEM problem has been well established in the literature. In this work, for the DEM model, an explicit time integration method is used to solve the translational and rotational motions of discrete particles.[65] For the CFD model, the finite volume method with the SIMPLE velocity-pressure coupling method[66] is used to solve the governing equations for gas phase by means of non-staggered grid arrangements in a body-fitted coordinate system.[67] The two-way coupling of particle and fluid flows is numerically achieved as follows. At each time step, DEM will give information, such as the positions and velocities of individual particles, for the evaluation of porosity and volumetric particle-fluid forces in a computational cell. CFD will then use these data to determine the gas-flow field, yielding the particle-fluid forces acting on individual particles. Incorporation of the resulting forces into DEM will provide information about the motion of individual particles for the next time step. This solution scheme has been well established since the work of Xu and Yu,[42] and is used in this work.

Simulation conditions

Table 2 shows the simulation conditions considered in this study. For each case, variables considered are gas velocity and/or solid-flow rate. Their varying ranges are listed in the table. The other parameters such as Young's modulus and Poisson ratio are constant, and the same as those used in our previous work.[49] For brevity, the following discussion is mainly based on the results of the base case (CASE I), and the results of other cases are used only in the last section to show the generality of the findings obtained according to the base case.

In the base case, in order to obtain typical flow regimes and corresponding pressure drop-gas velocity diagram in horizontal pneumatic conveying, the gas velocity is varied from 9.6 to 35.0 m/s for a constant solid-flow rate of 0.533 kg/m^3. The gas used is air, and its density is equal to 1.205 kg/m^3, and molecular viscosity is 1.85×10^{-5} kg/(m·s). A 3-D, 7-m long (L) horizontal pipe with internal diameter (D) of 0.0563 m is chosen as the computational domain. This corresponds to an L/D ratio of about 124. This ratio is large enough to obtain developed flows according to the work of Rao et al.,[23] who studied flow regimes in the horizontal pipe at the location 4 m ($L/D = 100$) away from the solid feeding point using tomography techniques. The computational domain is meshed with body-fitted grids, as illustrated in Figure 1. Its grid Scheme 8 × 8 × 800 is determined according to the grid-independence study used in a CFD study. The particles used in the base case are spherical, with dia. 3.18 mm, density 1180 kg/m^3, and restitution coefficient 0.8. These correspond to polyethylene pellets suited to the flow mode of dispersed flow, stratified flow, transition flow, and slug flow in horizontal pipes.[2,3] The aforementioned pipe diameter, particle density and gas- and solid-flow rates (CASE

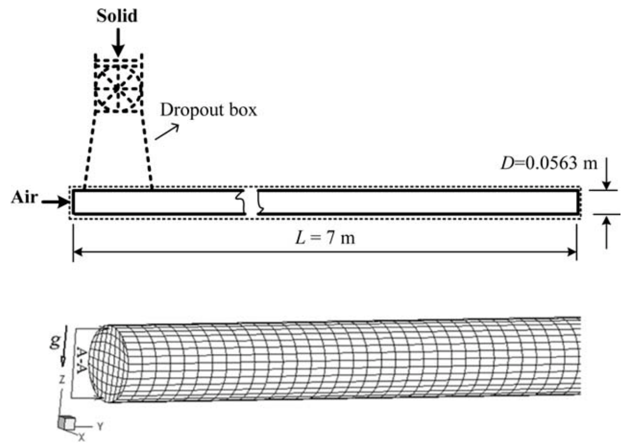

Figure 1. Schematic illustration of pipe geometry (top), and CFD mesh (bottom).

I) are based on the experimental work of Lecreps and Sommer,[3] and particle size corresponds to the equivalent size of oval polyethylene pellets used in their experiment. This allows us to make a meaningful comparison between the simulated and measured results.

In all simulations, particles are introduced through the top of the pipeline at a constant solid-flow rate with a small initial vertical velocity (downward), and zero velocity in two other directions, as used by Li et al.[68] This is to some extent similar to the feeding of particles into conveying pipelines from a rotary valve through a dropout box in practice (see Figure 1). Once moving out of the pipe, a particle will not be considered in the calculation. For gas flow, a fixed uniform velocity profile at the inlet is adopted, while the normal gradients of all variables at the outlet are set to zero assuming that the flow is fully developed. For DEM computation, the pipe wall is treated as rigid spheres with an infinite diameter and has no displacement and movement resulting from particle-wall interaction. A no-slip condition as used in the CFD is applied to gas phase at the pipe wall.

Each simulation lasts for 15 s, and the time step is 5×10^{-6} s. The simulation results are recorded every 0.01 s. Because macroscopically stable flow regimes are considered in this work, this analysis only involves simulation results under fully-developed conditions. The developed conditions are determined according to the temporal profile of average solid concentration over a cross-sectional area of the pipe, as shown by Kawaguchi et al.[69] and Kuang et al.[49] For example, based on such a principle, simulation data in the pipe section between $y = 5.7$ m ($L/D = 101$), and $y = 6.7$ m ($L/D = 119$) at the physical time from 4 to 15 s for all simulations of CASE I are chosen for this analysis. Here, the length of pipe section considered is determined according to the maximum length of slugs in the simulations.

Results and Discussion

The applicability of this CFD-DEM approach has been verified in our previous study, where quantitative agreement between simulated and measured results under different conditions is shown.[49] In this study, we will focus on the analysis of the flow regimes in horizontal pneumatic conveying. In the following, we will first show the flow regimes can be reproduced, then analyze the relative roles of various forces, and finally provide a new phase diagram.

Flow Regimes and their transition

When a material is transported in a specific system with varying gas velocities and a fixed solid-flow rate, the simplest method to describe the resulting flow regimes and flow transition is the phase diagram plotting pressure drop as a function of gas velocity. Figure 2 shows such a phase diagram simulated for the horizontal transport of polyethylene pellets, corresponding to CASE I. Note that the following discussions all refer to CASE I unless otherwise noted. In Figure 2, the pressure drops are the time-averaged values measured at the locations between $y = 5.7$ m and $y = 6.7$ m. It can be seen that when gas velocity is increased, the gas-only pressure drop increases, whereas with solids loaded at a fixed flow rate, the behavior of pressure drop becomes very complicated. First, the pressure drop decreases with increasing gas velocity. Further increase of gas velocity results in a sharp increase in pressure drop. The resulting pressure drop is much larger than all others (please refer to Figure 18), and is not plotted in Figure 2 for better showing the results. As gas velocity increases further, the pressure drop decreases to a normal level and gradually reduces to the minimum, and then increases slowly. Usually, the region to the right of the minimum is referred to as dilute-phase flow and the region to the left is dense-phase flow. This tendency is qualitatively consistent with the experimental measurements.[2,3,11,14] Note that quantitative comparison is not applicable because different particle shapes were used in the numerical and physical experiments, in addition to the uncertainties in CFD-DEM models related to the equations to calculate particle–particle and particle-fluid interaction forces, the selection of parameters for simulation.

Figures 3 and 4 show the temporal variations of solid concentration and pressure drop at different gas velocities, corresponding to Figure 2. Their typical solid-flow patterns are given in Figures 5–8. It can be seen from the figures that

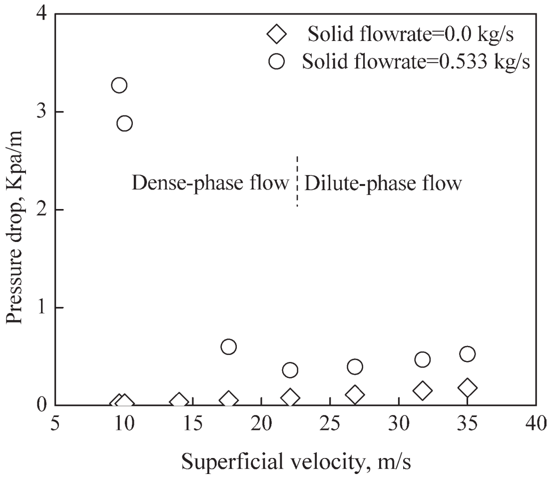

Figure 2. Pressure drop-gas velocity phase diagram for the transport of polyethylene pellets, for the section between $y = 5.7$ m and $y = 6.7$ m.

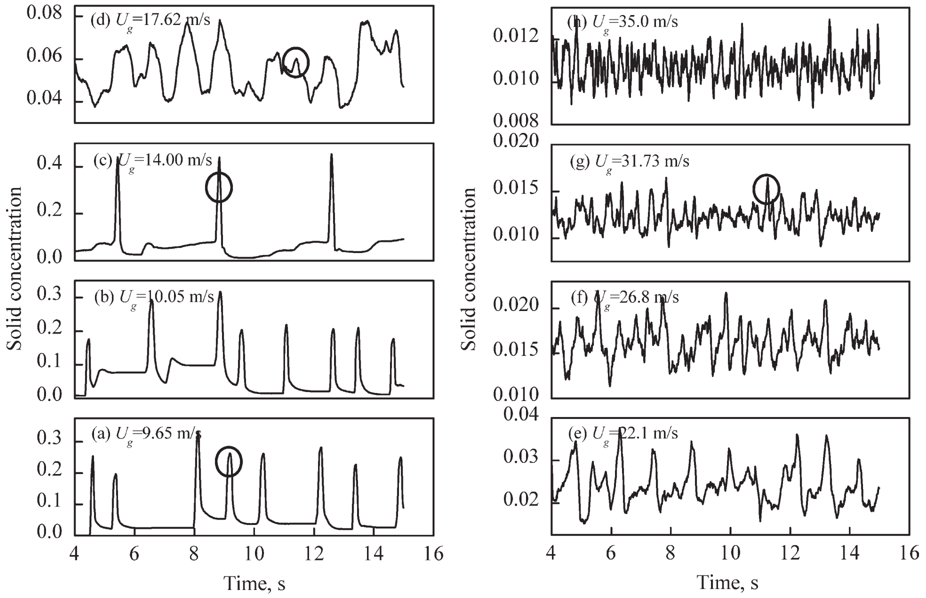

Figure 3. Temporal variation of solid concentration in the section between y = 5.7 and y = 6.7 m at different gas velocities, corresponding to Figure 2.

three flow modes, i.e., the slug-flow regime (Figure 5), the stratified flow regime (Figure 6), and the dispersed flow regime (Figure 7), and the transition flow between slug flow and stratified flow (Figure 8) can be numerically obtained for the horizontal transport of polyethylene pellets, as experimentally observed by Jama et al.[2] and Lecreps and Sommer.[3]

In the slug-flow regime, the entire cross area of the pipe is filled with particles in a slug, but with settled layers on the bottom in other parts of the pipe, as in the CCD camera records.[21,23,24] As a slug moves along the pipe, some particles are pushed ahead of the slug wave at the front, and this group of particles behave in a very dynamic and suspended fashion. This phenomenon has been experimentally confirmed in the work of Li et al.,[70] by analyzing video footages from experiments in slug flows using similar particulate materials (3 mm spherical polymer pellets). In addition, a pressure-drop peak and a solid-concentration peak always rise when a slug passes through the considered pipe (Figures 3a and 4a), and a large pressure drop usually corresponds to a long slug, which agrees well with the general observations of slug flow.[7,71–73] It also shows that the pressure-drop peak varies due to the unstable nature of slug flow (e.g., see Figures 4a). This is in line with the experimental observations by different investigators.[2,7,69]

In the stratified flow regime, a dense particle layer is formed in the lower portion of the pipe, with dunes or

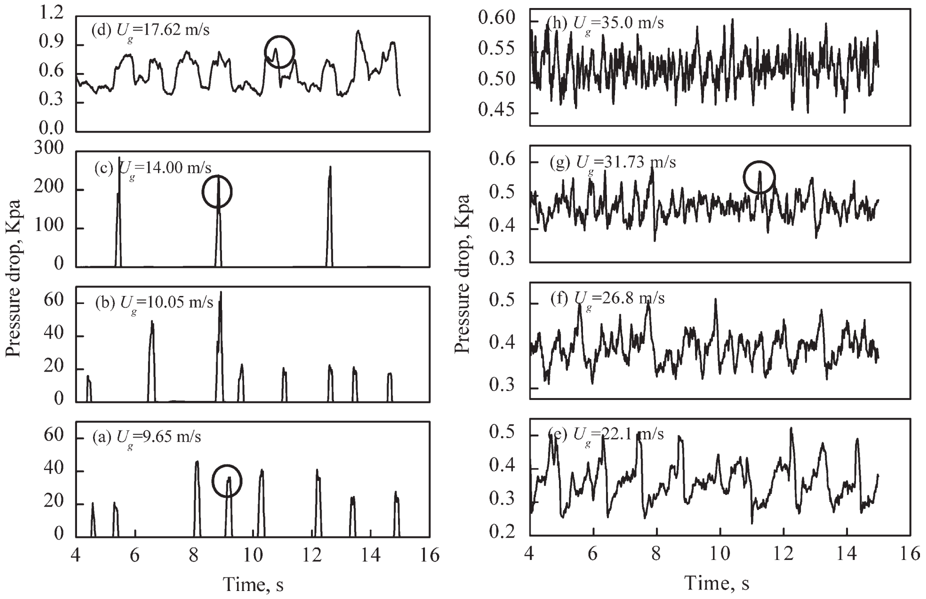

Figure 4. Temporal variation of pressure drop in the section between y = 5.7 and y = 6.7 m at different gas velocities, corresponding to Figure 2.

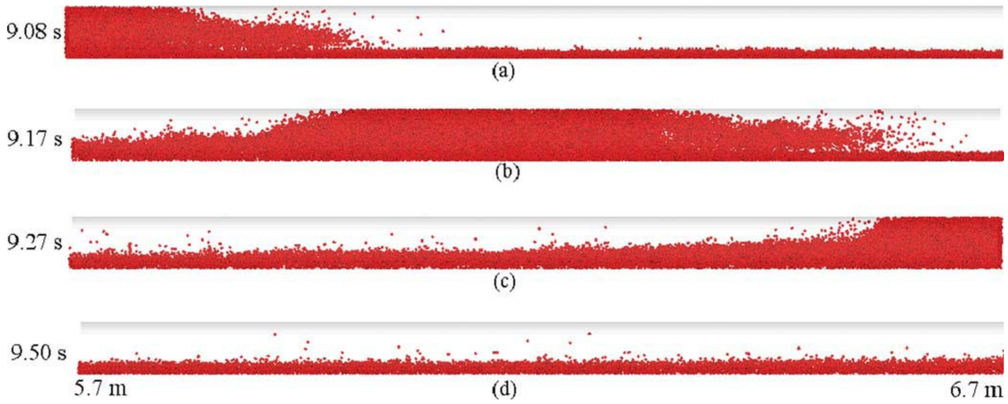

Figure 5. Snapshots showing typical solid-flow patterns in the section between *y* = 5.7 m and *y* = 6.7 m with *Ug* = 9.65 m/s, corresponding to the pressure drop and solid concentration labeled with circles in Figures 3a and 4a.

[Color figure can be viewed in the online issue, which is available at wileyonlinelibrary.com.]

clusters being observed from time to time (labeled by circles in Figure 6) as experimentally reported by Tsuji and Morikawa[10] and Jama et al.,[2] whereas in the upper portion of the pipe, a small number of particles are suspended in the transport gas. The dunes or clusters result in relatively large fluctuations of pressure drop and solid concentration (Figures 3d and 4d). These fluctuations become small and uniform in the dispersed flow regime (Figures 3g and 4 g) where the dunes or clusters cannot be observed and most of the particles are suspended in the pipe. Because coarse particles are considered in this work, gravity segregation is observed in the dispersed flow regime, i.e., particles in the lower portion of the pipe are generally denser than those in the upper portion, as shown in Figure 9c. Note that such segregation also exists in other flow regimes, but quantitatively different flow regimes give different results (Figure 9).

Figures 3 and 4 also demonstrate how the slug flow regime transits into the dispersed flow regime with the increase of gas velocity. Overall, an unsmooth transition[12] is numerically obtained as expected for the horizontal transport of polyethylene pellets. When the gas velocity is increased in the range from 9.65 to 10.05 m/s, the flows belong to the slug-flow regime, where most of the slugs decrease in length with the increase of gas velocity. This leads to reduced average pressure drop and pressure fluctuation peak, as shown in Figure 3a and 3b. One may note that in the slug-flow regime, the flow at higher gas velocities sometimes has pressure peaks higher than those at low-gas velocities (Figure 4a and 4b). This result is reasonable according to the experimental studies of Jama et al.[2] and Lecreps and Sommer,[3] where some slug flows even show higher average pressure drop for higher gas velocity. This reflects another side of the unstable nature of the slug flow.

Increasing gas velocity after the slug-flow regime leads to transition flows featured with very large high-pressure fluctuations and particles deposit,[2,11,12,14] which causes expensive computer power in simulations. Therefore, only one gas velocity for such a flow is considered, and the resulting results are given by Figures 3c, 4c and 8. It can be seen from Figure 4c that the pressure peaks in the transition flow are about 3-4 times larger than those in the slug-flow regime. This pressure may be beyond the blower capability or produce large fluctuations in practical pneumatic conveying, leading to the blockage of conveying pipeline. As such, the transition flow is usually referred to as unstable flow, although the slug-flow regime may also to some extent exhibit an unstable nature, as discussed earlier. Note that the aforementioned blockage never happens in our simulations, because unlike some of physical experiments, the inlet flow rate of gas in the CFD can always remain constant and there is no limit to pressure drop. The high-pressure peaks in the transition flow considered in this study stem from long slugs in the conveying pipeline, as shown in Figure 8. It can be seen from the figure that with time evolution, a small slug is formed near

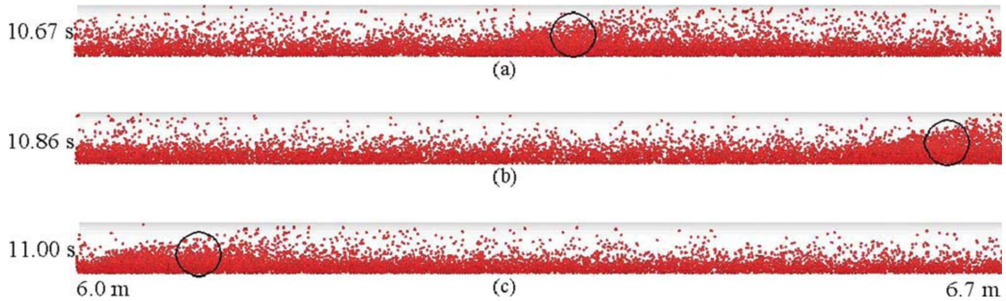

Figure 6. Snapshots showing typical solid-flow patterns in the section between *y* = 5.7 m and *y* = 6.7 m with *Ug* = 17.62 m/s, corresponding to the pressure drop and solid concentration labeled with circles in Figures 3d and 4d.

[Color figure can be viewed in the online issue, which is available at wileyonlinelibrary.com.]

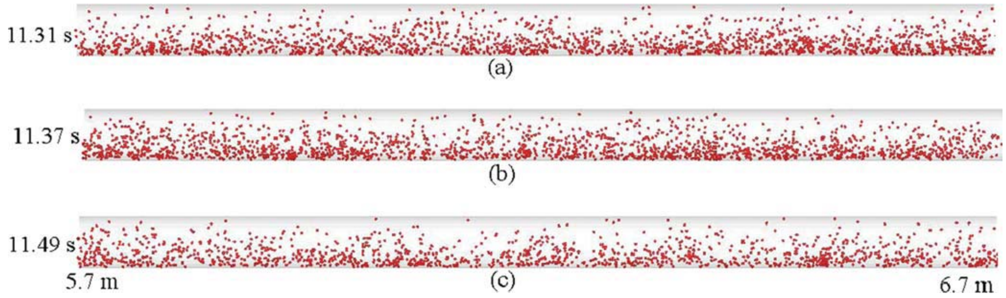

Figure 7. Snapshots showing typical solid-flow patterns in the section between $y = 5.7$ m and $y = 6.7$ m with $Ug = 31.73$ m/s, corresponding to the pressure drop and solid concentration labeled with circles in Figures 3g and 4 g.

[Color figure can be viewed in the online issue, which is available at wileyonlinelibrary.com.]

the inlet region in the stratified flow regime (Figures 8a and 8b), and then increases gradually in length when moving to the outlet (Figure 8c), and finally becomes a long slug (Figure 8e). The formation of a long slug is attributed to the fact that as the slug moves, it picks up a relatively thick layer of material in front of it, but only deposits a thin layer behind it (see Figures 3c, 8d and 8f). These phenomena are the same as those reported in the experimental work of Wypych and Yi.[11] Interestingly, it is found that the development of a long slug periodically repeats (Figures 3c and 4c); however, this is not observed in the transition flows for CASE II and CASE III. The related reason is not clear due to our limited simulation data obtained for the transition flow. It will be investigated in the future.

As gas velocity increases further, slugs can no longer be observed. The flow exists stably in the stratified flow regime, and then develops smoothly from this flow regime to the dispersed flow regime, featured with smooth decrease of pressure fluctuation, and more and more particles being suspended in the transport gas. These flow behaviors result in difficulty in identifying the boundary between the stratified flow regime and the dispersed flow regimes based on flow visualization or variation of pressure drop.

Force analysis

Key Features of the Forces on Particles. According to Eqs. 1 and 2, the motion of a particle is governed by various particle–particle, particle-wall, and particle-fluid interaction forces, in addition to the gravity forces. Analysis of these forces should, hence, generate some insight into particles behavior, leading to a better understanding of flow regimes and their transitions. Such analysis is difficult to achieve experimentally but can be readily performed based on this CFD-DEM simulations.

Figures 10–12 show the typical forces and relevant flow information calculated in the slug-flow regime, the stratified flow regime, and the dispersed flow regime. For better

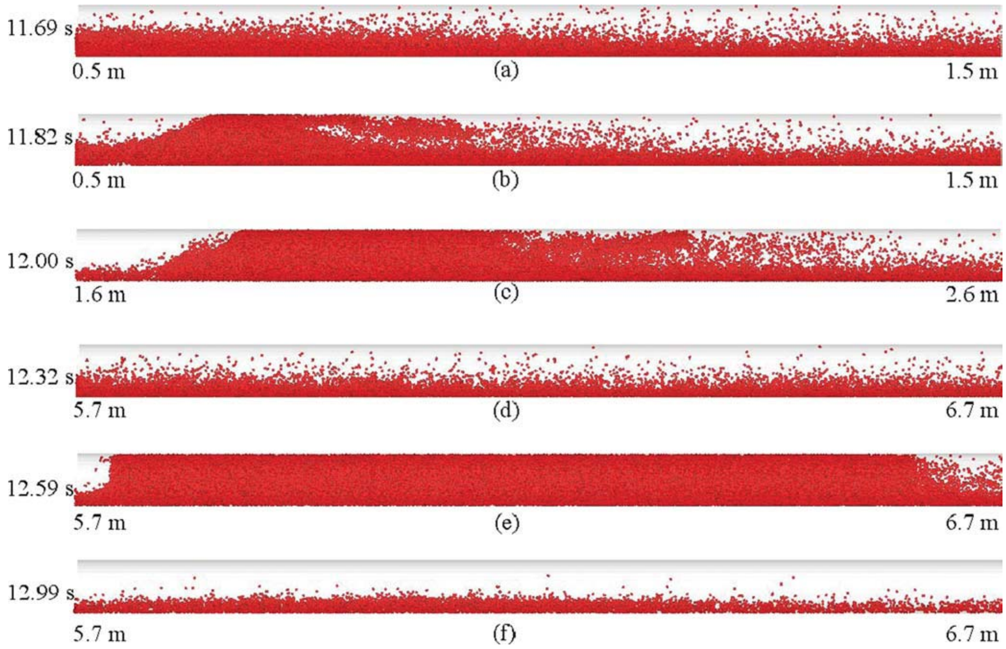

Figure 8. Snapshots showing typical solid-flow patterns in the section between $y = 5.7$ m and $y = 6.7$ m with $Ug = 14.0$ m/s, corresponding to the pressure drop and solid concentration labeled with circles in Figures 3c and 4c.

[Color figure can be viewed in the online issue, which is available at wileyonlinelibrary.com.]

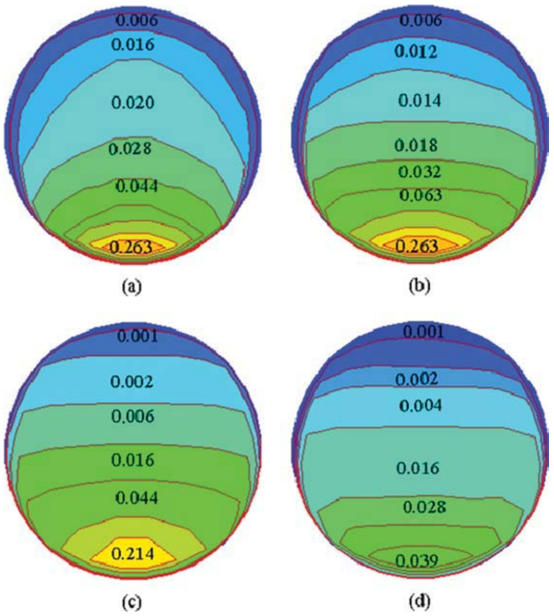

Figure 9. Time-average solid concentration in the cross-sectional area of the pipe for the section between *y* = 5.7 m and y = 6.7 m: (a) slug flow, (b) transition flow, (c) stratified flow, and (d) dispersed flow; they correspond to Figures 5-8, respectively.

[Color figure can be viewed in the online issue, which is available at wileyonlinelibrary.com.]

visualization, only particles whose center points are between $x = -6.36 \times 10^{-3}$ m, and $x = 6.36 \times 10^{-3}$ m (near the vertical central A-A plane in Figure 1) are presented here, and the side view is shown. The results in the figures include the spatial distributions of solid concentrations, radial gas velocity, axial gas velocity, gas-pressure drop along the pipeline, axial particle velocity, axial fluid drag forces, axial pressure gradient forces, and particle–particle forces. These correspond to particle configures at different times. Here the radial results, which are small and not major factors accounting for the transport of particles along the pipeline, are not considered for brevity, and to be dimensionless, the magnitude of the forces shown are expressed relative to the gravity force of a particle.

It can be seen from Figure 10a that in the slug-flow regime, particles inside a slug are densely packed, with uniform solid concentration around 0.58 near the center of the pipe and a slightly lower value near the wall. In addition, the head of the slug and the front settled layer, respectively, have solid concentrations which are denser than those on the tail and the back settled layer. Correspondingly, the gas velocity inside the slug is uniform near the center of the pipe, but with a higher value near the wall (Figure 10c). In contrast, only partial flows can be observed outside the slug, featured with a relatively large axial gas velocity over the settled layers. Furthermore, the axial gas velocity in the back settled layer is larger than that in the front settled layer. Overall, the radial gas velocity is negligible compared to the axial gas velocity, having a random direction (Figure 10b). This is also the case for other flow regimes (Figures 11b and 12b). Figure 10b also shows that the radial gas velocity remains negative near the slug tail, but positive near the slug head, as observed in other studies.[58] Different from the velocity distribution, the pressure drop mainly happens inside the slug along the pipe, and is negligible outside the slug (Figure 10d), similar to that observed by Tomita et al.[73] Because of the aforementioned flow properties of gas phase, the fluid-drag force shown in Figure 10f, and the pressure gradient force shown in Figure 10g, is both several times the particle gravity force inside the slug and less than particle gravity force inside the settled layers and other parts. Interestingly, it is found that the pressure gradient force has a more uniform distribution in the radial direction than the fluid-drag force, similar to those found in a vertical slug flow.[49] Note that the radial particle-fluid force, which is not presented for brevity, is generally much smaller than the particle gravity force. These features of particle-fluid forces are believed to result in the distribution of particle velocities given in Figure 10e. As can be seen from the figure, the axial particle velocity is close to zero in the front settled layer and becomes large inside the slug, and is smaller in the back settled layer. Actually, particles in the back settled layer gradually settle down when the slug moves away. For comparison, the particle–particle force, as the driving force of a slug for picking up particles in its front settled layers,[58] is given in Figure 10h. It can be seen that the particle–particle force is mainly distributed near the middle section of the slug, and can be a thousand times the particle gravity force. Such a force is inclined to the horizontal direction and directed downward on the slug head, as highlighted in Figure 10h. This is the same as that observed in other studies.[58] Here, the particle–particle force is the normal contact force which is the major particle–particle force resulting from the interactions between particles.

Figure 11a shows that in the stratified flow regime, solid concentration in the dense layer except for the dune or cluster (labeled by a circle), is looser than that in the settled layers of slug flow. Because of the presence of the dune with dense-solid concentration (~0.4), the gas passage at the location of the dune becomes narrow. Consequently, the partial flow of gas phase in the stratified flow is pronounced near the front of the dune, featured with a large axial gas velocity (Figure 11c). As expected, the radial gas velocity is positive and becomes relatively large near the back of the dune (Figure 11b). This causes a sudden change of pressure drop along the pipe as shown in Figure 11d, which accounts for the big fluctuation of pressure in the stratified flow regime, as experimentally reported by Tomita et al.[73] Otherwise, a linear pressure drop is achieved. Figure 11c also shows that, compared to the settled layers of slug flow, the dense layer of stratified flow has a larger axial gas velocity. Even so, the axial fluid-drag force in the dense layer is below particle gravity (Figure 11f). In contrast, the suspended particles over the dense layer obtain fluid-drag forces larger than particle gravity, although still smaller than those on the particles inside a slug (Figure 10f). In the stratified flow regime, the pressure gradient forces are generally decreased to the values far below particle gravity, even in the dune (Figure 11g), and the particle–particle forces decrease sharply, and distribute mainly in the dense layer (Figure 11h). In general, the axial velocities of particles are increased, and have a non-uniform distribution in the

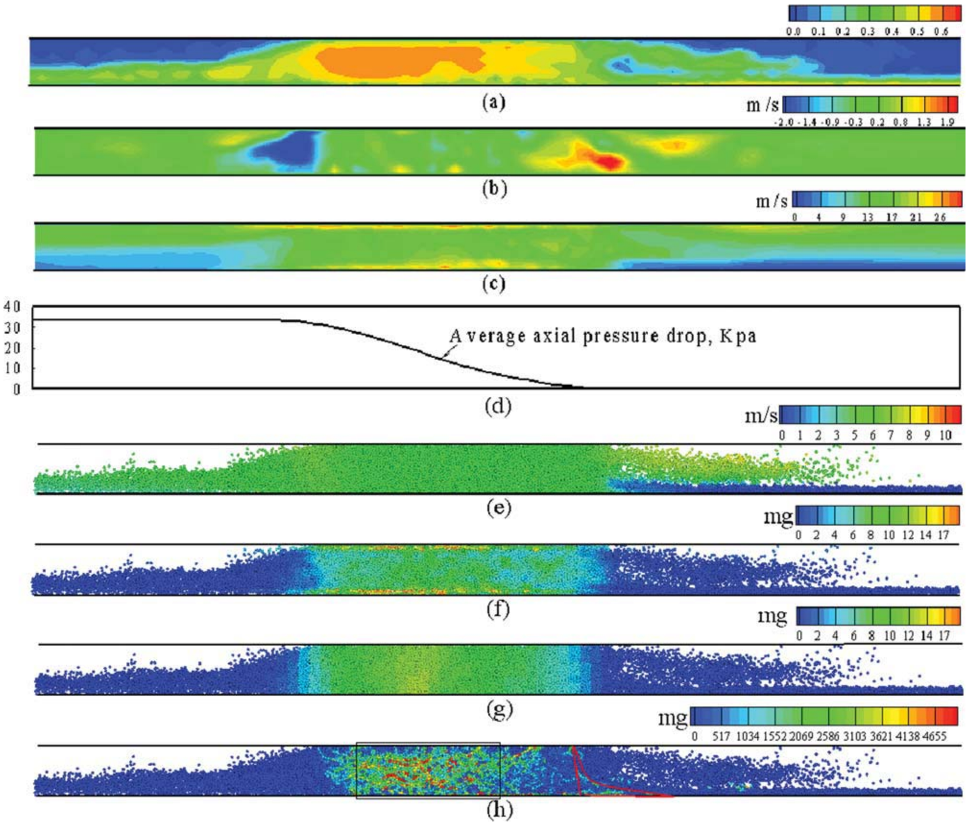

Figure 10. Snapshots showing the spatial distributions of forces on particles and the related flow properties on the A-A sectional plane for the slug-flow regime: (a) solid concentration; (b) radial gas velocity; (c) axial gas velocity; (d) average axial pressure drop along the pipeline; (e) axial particle velocity; (f) axial fluid-drag force; (g) axial pressure gradient force; (h) normal contact force, corresponding to Figure 5b.

In this figure (and Figures 11 and 12), mg denotes the gravity of a particle and is the units of the forces shown. [Color figure can be viewed in the online issue, which is available at wileyonlinelibrary.com.]

gravitational direction, with their magnitudes gradually increasing from the bottom to the top (Figure 11e).

Figure 12 shows that in the dispersed flow regime, solid concentration is relatively dilute (< 0.1) (Figure 12a), and the uniformity of particles in the gravitational direction is evidently improved, compared to the stratified flow regime. This tendency also happens to the axial gas velocity and the axial particle velocity (Figure 12c). In addition, the pressure drop is observed to decrease along the pipe linearly and smoothly (Figure 12d). This leads to negligible pressure gradient forces on particles (Figure 12g). In contrast to the pressure gradient forces, the fluid drag forces on all particles except for those very close to the pipe walls are larger than particle gravity forces (Figure 12f). Because of the low-solid concentration in the dispersed flow regime, particle–particle interaction becomes occasional, and mainly in the lower portion of the pipe (Figure 12h).

Roles of the Forces in the Pressure Drop-Gas Velocity Phase Diagram. The pressure drop in pneumatic conveying is composed of the gas-only pressure and the pressure drop due to the presence of solid particles.[74] Our previous study[49] suggests that these two subpressure drops can, respectively, be directly estimated according to the gas-wall friction force and the particle-fluid force in vertical pneumatic conveying, and, thus, the pressure behavior can be further evaluated in terms of forces and related parameters. This finding is examined using horizontal pneumatic conveying in this work. For such a purpose, the definition of average volumetric particle-fluid over a period of time as previously proposed[49] is introduced, given by

$$\frac{1}{\Delta t}\sum_{\Delta t}\left[\frac{1}{V_{\text{section}}}\left(\sum_{i=1}^{N_{p,\text{section}}}\mathbf{f}_i\right)\right] \tag{6}$$

where $\mathbf{f}_i$ represents the fluid-drag force or pressure gradient force acting on particle i, $N_{p,\text{section}}$ and V_{section} are the number of particles in a considered pipe section and the volume of the pipe section, respectively.

Figure 13 shows the average volumetric fluid drag force, pressure gradient force, gas-wall friction force, and the sum of the three forces as a function of gas velocity. Here, the volumetric gas-wall friction force is estimated by the pressure drop of gas flow in an empty pipe.[75] It can be seen from Figure 13 that as gas velocity increases, the fluid-drag force decreases in the slug-flow regime, but increases to a large value in the transition flow, and then decreases to a normal level and gradually reduces to a minimum, followed

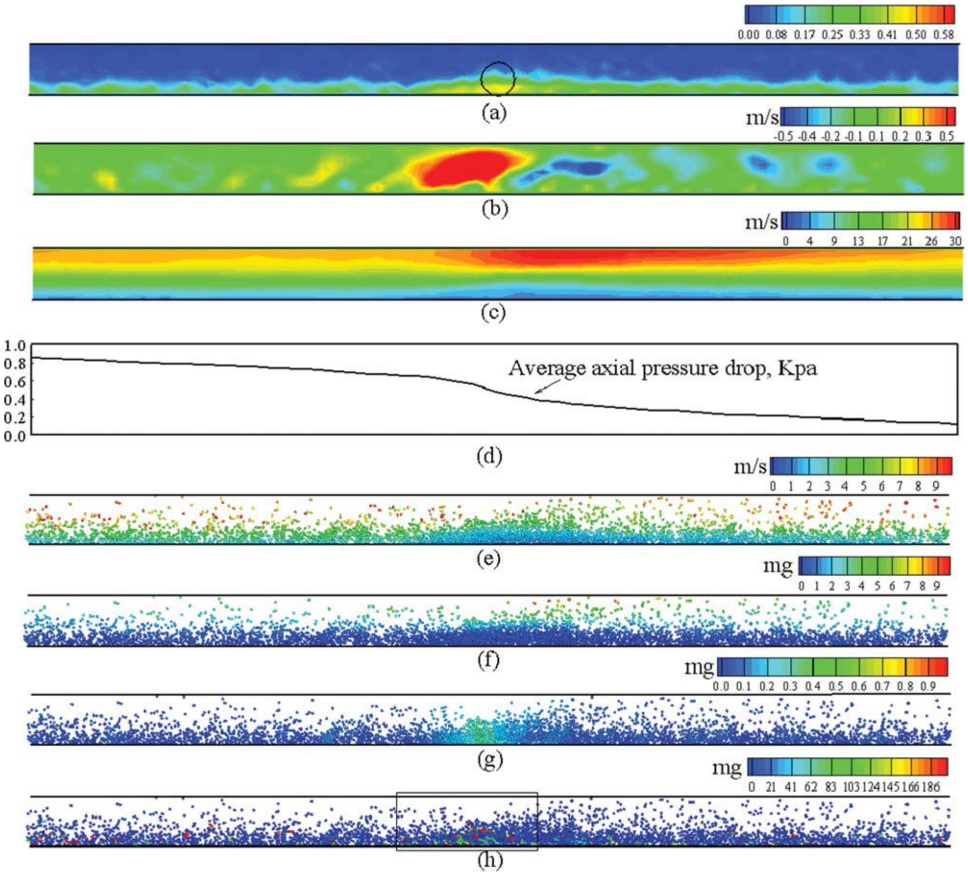

Figure 11. Snapshots showing the spatial distributions of forces on particles and the related flow properties on the A-A sectional plane for the stratified flow regime: (a) solid concentration; (b) radial gas velocity; (c) axial gas velocity; (d) average axial pressure drop along the pipeline; (e) axial particle velocity; (f) axial fluid-drag force; (g) axial pressure gradient force; (h) normal contact force, corresponding to Figure 6a.

[Color figure can be viewed in the online issue, which is available at wileyonlinelibrary.com.]

by a slight increase. The pressure gradient force is almost the same as the fluid drag force in the slug-flow regime and the transition flow; however, it becomes very small (close to zero) in both the stratified flow regime and the dispersed flow regime. In contrast, the gas-wall friction increases in an almost linear way. It appears that the tendencies of the three forces are different from that of pressure drop shown in Figure 2. However, one may note that the curve for the sum of the three forces is quantitatively equal to the pressure drop given in Figure 2. Therefore, it can be concluded that in horizontal pneumatic conveying, the pressure drop can also be estimated using the particle-fluid force and gas-wall friction force, as done in vertical pneumatic conveying. Based on such a finding, it can be seen from Figure 13 how the particle-fluid forces and gas-wall friction force contribute to the pressure behaviors in Figure 2. Evidently, in the slug-flow regime and the transition flow, the pressure drop is determined by the pressure gradient force and the fluid-drag force. However, in the stratified-flow regime and the dispersed-flow regime, the pressure drop is mainly controlled by the fluid-drag force and the gas-wall friction.

The fluid-drag force or the pressure drop related to the fluid drag can be further analyzed in relation to the gas and solid-flow structure. By definition, it is a function of solid concentration and relative velocity between gas and particle. Figure 14 shows how the two factors vary with gas velocity. Here the average relative velocity over a period of time is calculated by

$$\frac{1}{\Delta t}\sum_{\Delta t}\left\{\frac{1}{V_{\text{section}}}\left[\sum_{i=1}^{N_{p,\text{section}}}(\mathbf{u}_i-\mathbf{v}_i)\right]\right\} \qquad (7)$$

It can be seen from the figure that with increasing gas velocity, the relative velocity between particles and gas increases linearly, whereas solid concentration rapidly decreases initially and then slows down. In contrast to particle-fluid forces, neither solid concentration nor relative velocity can be used to directly identify the transition flow. This may be due to the fact that the average solid concentration alone can only reflect how many particles are located in the considered pipe section, not the number of particles transported along the pipeline. The latter is more related to the characteristics of pressure drop in different flow regimes. A similar problem exists in the average particle velocity. In addition, the role of pressure gradient is heavily dependent on the structures of flow regimes, and

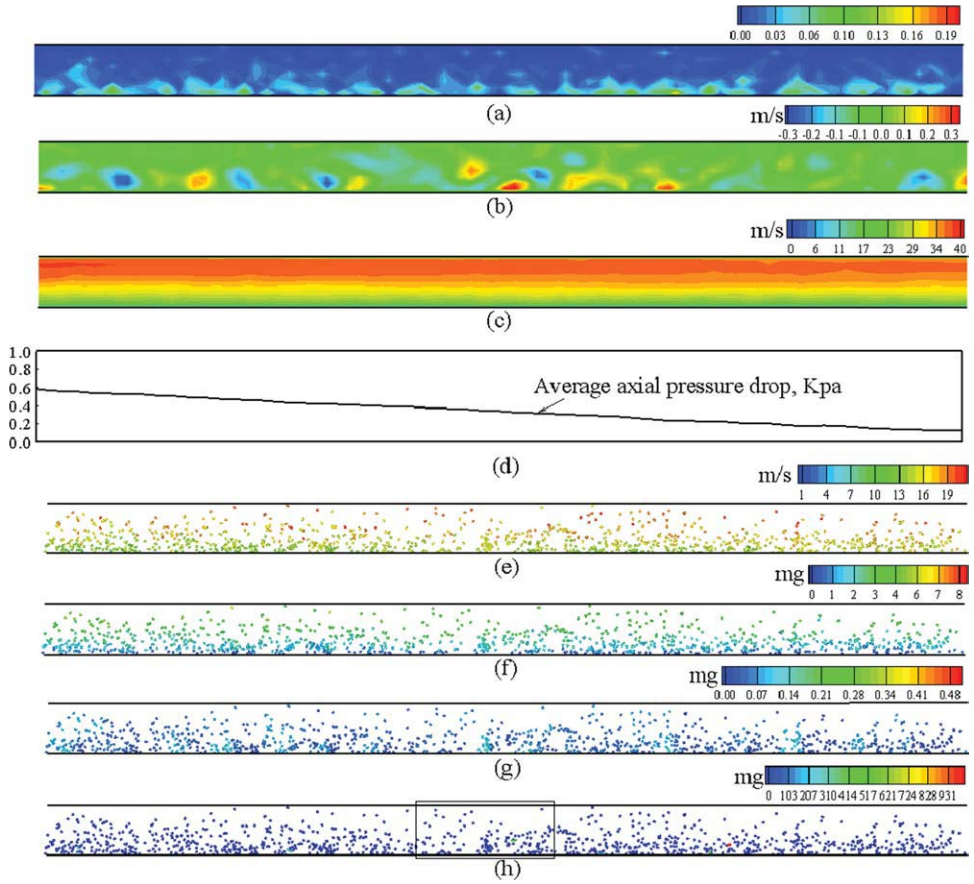

Figure 12. Snapshots showing the spatial distributions of forces on particles and the related flow properties on the A-A sectional plane for the dispersed flow regime: (a) solid concentration; (b) radial gas velocity; (c) axial gas velocity; (d) average axial pressure drop along the pipeline; (e) axial particle velocity; (f) axial fluid-drag force; (g) axial pressure gradient force; (h) normal contact force, corresponding to Figure 7b.

[Color figure can be viewed in the online issue, which is available at wileyonlinelibrary.com.]

cannot be reflected by average solid concentration and particle velocity.

New Phase Diagram. The pressure drop-gas velocity phase diagram (Figure 2) focuses on pressure drop which is related to gas phase only. It indirectly reflects how a gas–solid flow behaves in pipelines. Consequently, such a diagram may not correspond well to a visualized particle flow pattern and has limitations in its application, as discussed earlier. To overcome this problem, we have attempted to use the forces governing particle motions to directly describe particle behavior in pneumatic conveying. That is, we try to establish a new phase diagram in terms of the forces governing the particle flow.

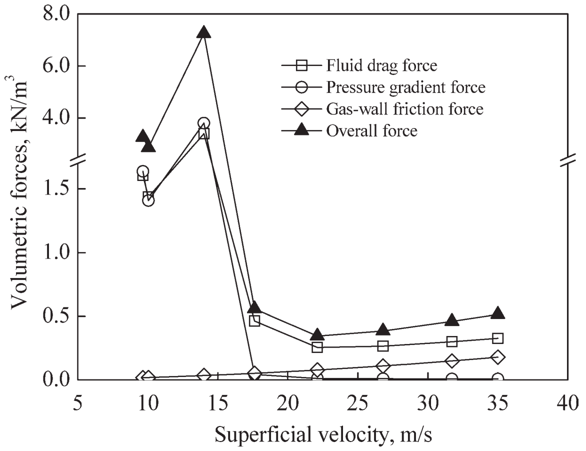

Figure 13. Average volumetric fluid drag force, pressure gradient force and gas-wall friction force as a function of gas velocity.

Following our recent studies on pneumatic conveying,[49,58] we analyze particle–particle, particle-fluid and particle-wall forces at two scales: pipe scale and particle scale. The pipe-scale analysis considers forces acting on a sectional pipe, whereas the particle-scale analysis focuses on forces acting on an individual particle. At the pipe scale, the volumetric average particle–particle force over a period of time can be calculated by

$$|\mathbf{F}|_{\text{pipe}} = \left|\frac{1}{\Delta t}\sum_{\Delta t}\left\{\frac{1}{V_{\text{section}}}\left[\sum_{i=1}^{N_{p,\text{section}}}\left(\sum_{j=1}^{k_i}\mathbf{f}_{cn,ij}+\mathbf{f}_{dn,ij}+\mathbf{f}_{ct,ij}+\mathbf{f}_{dt,ij}\right)\right]\right\}\right| \tag{8}$$

The force, as an internal interaction within a particle assembly is equal to zero, because they can be cancelled out according to Newton's third law of motion. However, this

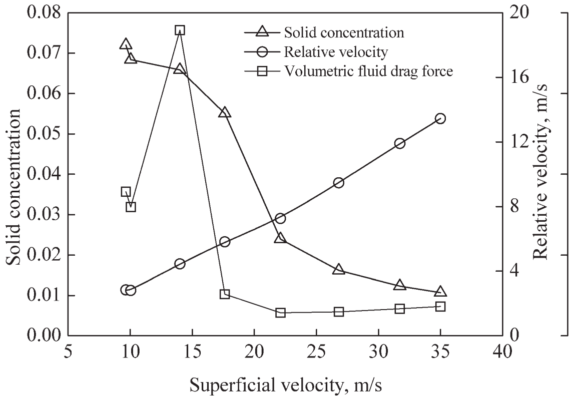

Figure 14. Average solid concentration and relative velocity of gas to particle as a function of gas velocity.

does not hold for the particle–particle force at a particle scale, which is here expressed as

$$|\mathbf{F}|_{\text{particle}} = \frac{1}{\Delta t}\sum_{\Delta t}\left\{\frac{1}{V_{\text{section}}}\left[\sum_{i=1}^{N_{p,\text{section}}}\left(\sum_{j=1}^{k_i}\left|\mathbf{f}_{cn,ij}+\mathbf{f}_{dn,ij}+\mathbf{f}_{ct,ij}+\mathbf{f}_{dt,ij}\right|\right)\right]\right\} \tag{9}$$

Equation 9 can also apply to the calculation of the particle-wall interaction force, with particle j replaced by a wall. Figure 15 shows the so obtained volumetric average particle–particle and particle-wall forces. To be consistent, the sectional pipe considered here is the same as that used in the aforementioned discussions. It can be seen from the figure that as gas velocity increases, the particle-wall and the particle–particle forces both decrease rapidly in the slug-flow regime, but increase to a large value in the transition flow regime, and then decrease to a normal level and finally reduce gradually. The results indicate that the particle-wall force is always dependent on the particle–particle force in this conditions, or vice versa. This dependence remains the same at high-gas velocities, unlike vertical pneumatic conveying where the particle-wall force may become more and more independent of the particle–particle force with increasing gas velocity.[49] This can be explained later. In the slug, transition, and stratified flow regimes, the particle–particle interaction can transfer to pipe wall through the contacts between particles, which can be demonstrated by the network of the normal contact forces given in Figure 16a and 16b. Note that here the force network of the transition flow is not given as it is similar to that of slug flow. Such a force network cannot be established in the dispersed flow regime as the particles are very dilute and thus have only a few occasional collisions (Figure 16c). However, because of the gravity force, particles hit by other particles in a horizontal pipe have higher chance of hitting pipe wall than those in a vertical pipe. Thus, the relation between the particle–particle force and particle-wall force is stronger in horizontal pneumatic conveying.

The forces on a particle or a particle assembly can be generally classified into three categories. These are the particle-fluid force which here is the sum of the fluid drag and pressure gradient forces, the particle–particle and particle-wall forces (the two are grouped together because they behave similarly and are of the same nature), and the gravity force. This will produce two dimensionless numbers, $\prod_1$ and $\prod_2$, given by:

(a) at the pipe scale

$$\prod\nolimits_{1,\text{pipe}} = \frac{\left|\frac{1}{\Delta t}\sum_{\Delta t}\left\{\frac{1}{V_{\text{section}}}\left[\sum_{i=1}^{N_{p,\text{section}}}\left(\sum_{j=1}^{k_i+k_w}\mathbf{f}_{cn,ij}+\mathbf{f}_{dn,ij}+\mathbf{f}_{ct,ij}+\mathbf{f}_{dt,ij}\right)\right]\right\}\right|}{\frac{1}{\Delta t}\sum_{\Delta t}\left[\frac{1}{V_{\text{section}}}\left(\sum_{i=1}^{N_{p,\text{section}}} mg_i\right)\right]} \tag{10a}$$

and

$$\prod\nolimits_{2,\text{pipe}} = \frac{\left|\frac{1}{\Delta t}\sum_{\Delta t}\left[\frac{1}{V_{\text{section}}}\left(\sum_{i=1}^{N_{p,\text{section}}}\mathbf{f}_{\text{drag},i}+\mathbf{f}_{pgf,i}\right)\right]\right|}{\frac{1}{\Delta t}\sum_{\Delta t}\left[\frac{1}{V_{\text{section}}}\left(\sum_{i=1}^{N_{p,\text{section}}} mg_i\right)\right]} \tag{10b}$$

(b) at the particle scale

$$\prod\nolimits_{1,\text{particle}} = \frac{\frac{1}{\Delta t}\sum_{\Delta t}\left\{\frac{1}{V_{\text{section}}}\left[\sum_{i=1}^{N_{p,\text{section}}}\left(\sum_{j=1}^{k_i+k_w}\left|\mathbf{f}_{cn,ij}+\mathbf{f}_{dn,ij}+\mathbf{f}_{ct,ij}+\mathbf{f}_{dt,ij}\right|\right)\right]\right\}}{\frac{1}{\Delta t}\sum_{\Delta t}\left[\frac{1}{V_{\text{section}}}\left(\sum_{i=1}^{N_{p,\text{section}}} mg_i\right)\right]} \tag{11a}$$

and

$$\prod\nolimits_{2,\text{particle}} = \frac{\frac{1}{\Delta t}\sum_{\Delta t}\left[\frac{1}{V_{\text{section}}}\left(\sum_{i=1}^{N_{p,\text{section}}}\left|\mathbf{f}_{\text{drag},i}+\mathbf{f}_{pgf,i}\right|\right)\right]}{\frac{1}{\Delta t}\sum_{\Delta t}\left[\frac{1}{V_{\text{section}}}\left(\sum_{i=1}^{N_{p,\text{section}}} mg_i\right)\right]} \tag{11b}$$

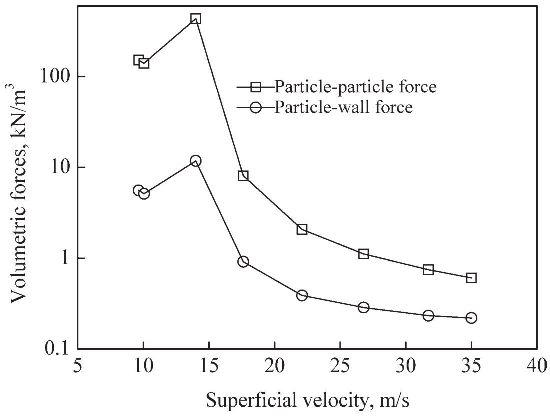

Figure 15. Average volumetric particle-particle and particle-wall forces as a function of gas velocity.

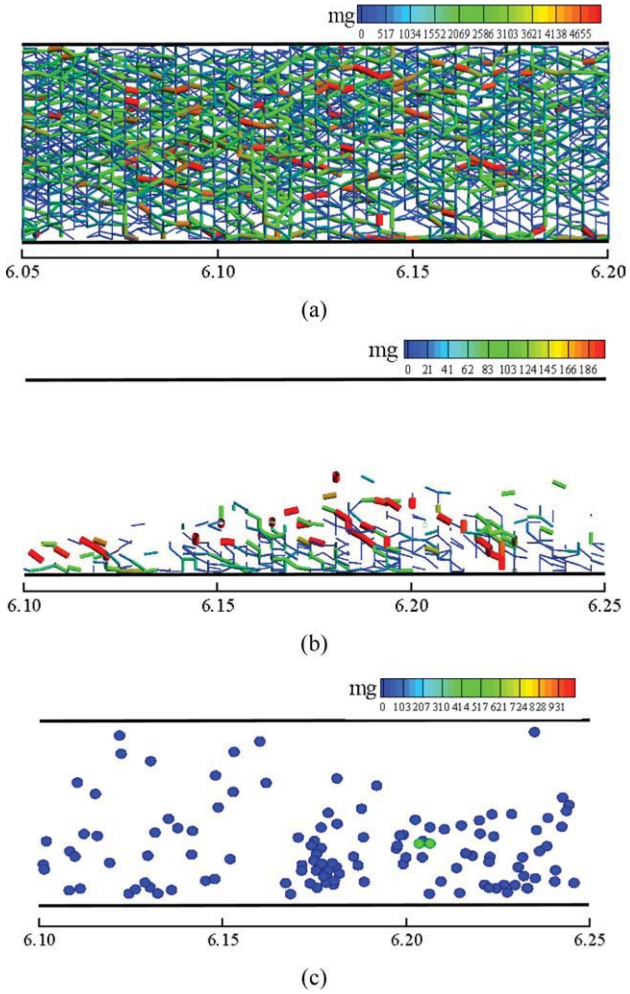

Figure 16. Snapshots showing network of normal contract force in (a) the slug-flow regime and (b) the stratified flow regime, and (c) spatial distribution of normal contact force in the dispersed flow regime, for squared regions in Figures 10g, 11g and 12g, respectively.

[Color figure can be viewed in the online issue, which is available at wileyonlinelibrary.com.]

Figure 17 shows the phase diagram in terms of the two dimensionless numbers. It can been seen from the figure, that no matter whether at a pipe scale or a particle scale, the phase diagrams can give the same message. There are two regions: the particle–particle or particle-wall interaction is almost constant at the smallest value in the left region, but increases with the increase of $\prod_2$ in the right region, and the boundary of the two regions is located at the minimum of $\prod_1$. The stratified flow regime and the dispersed flow regime are located in the left region, while the slug and transition flow regimes belong to the right region. This is slightly different from the pressure drop-gas velocity phase diagram (Figure 2), where two regions, i.e., dilute-phase flow and dense-phase flow also exist, but to which region the stratified flow regime belongs may depend on the conditions considered, as reported in the experiments of Jama et al.[2] and Lecreps and Sommer.[3] Moreover, it is of interest to find that in Figure 17 the transition flow and the slug-flow regime are in the same straight line, although the distance between them is distinctly large. However, in Figure 2 the transition flow deviates greatly from the curve of slug flow. Notably, the new diagram for horizontal pneumatic conveying are similar in profile to that for vertical pneumatic conveying,[49] although flow regimes in horizontal pipes are much more complicated. However, their curves are different in position due to the different effects of gravity force on flow regimes, which are not taken into account by the dimensionless numbers used.

Effects of other parameters

It is known that flow regimes in pneumatic conveying are affected by many variables related to material properties, operating conditions, and pipe geometries. It would be of interest to examine how the change of any of such variables affects the aforementioned findings. This will need a systematic study that is far beyond the current research effort because the number of variables is quite large. Nonetheless, we consider other four cases and vary some variables as listed in Table 2 to examine if our findings, particularly

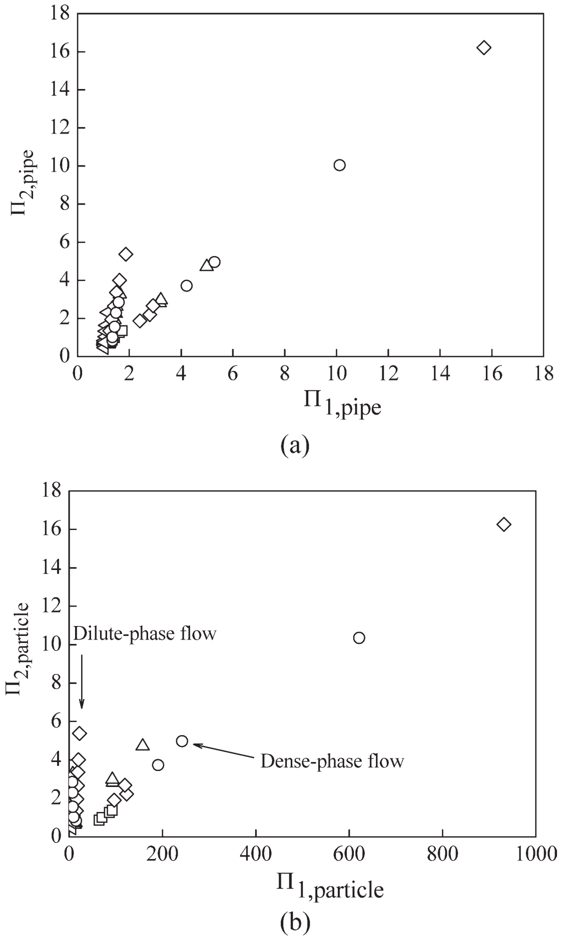

Figure 17. Phase diagram in terms of the forces on particles: (a), at the pipe scale; and (b), at the particle scale; ○ CASE I, △ CASE II, ◇ CASE III, □ CASE IV, ◁ CASE VI.

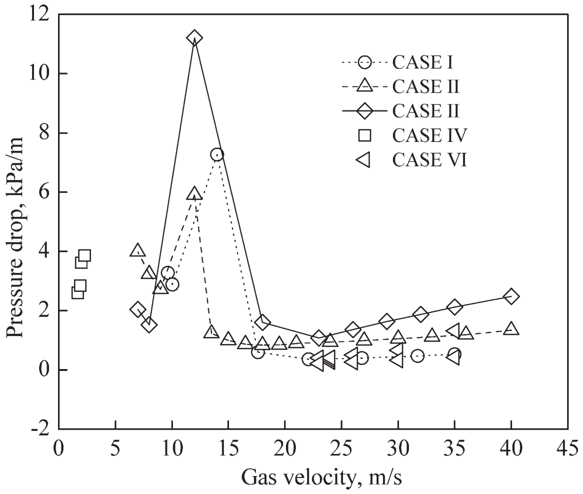

Figure 18. Phase diagram of horizontal pneumatic conveying corresponding to the conditions listed in Table 2.

those related to the new phase diagram, are affected under different conditions.

In CASE II and CASE III, the gas velocity is varied at a fixed flow rate to obtain different flow regimes, as done in CASE I. Other key parameters such as pipe size and particle properties are constant but different from those in CASE I (see Table 2). As expected, the slug-flow regime, the transition flow, the stratified flow regime, and the dispersed flow regime are obtained in both cases. The corresponding pressure characteristics are plotted in Figure 18, where the results of CASE I are also given for comparison. It can be seen from the figure that the characteristics of pressure drops are similar for the three cases. Their solid-flow patterns and the forces acting on particles are also similar, which are not presented for brevity. These results are reasonable as the flow conditions in the three cases are close to each other to some degree.

Other two extreme cases are also considered in order to examine these findings, which involve only low-gas velocities (CASE IV), and high-gas velocities (CASE VI), respectively. In CASE IV, the gas velocity ranges from 1.7 m/s to 2.3 m/s, where only the slug flow regime is obtained. Because of the low-gas velocity, the number of particles used in the simulation is large, which is very demanding in computation. Periodic boundary conditions (PBC) are, hence, applied to both gas and particles in the flow direction to improve computational efficiency, as done elsewhere.[58] It should be pointed out that at this stage of development; there is a difficulty in applying the PBC treatment generally. The problem is that in such a CFD-DEM simulation, the number of particles is preset, which gives different solid-flow rates when gas velocity and other pneumatic conveying conditions vary.[58] It is difficult to control solid-flow rate when PBC is used. In this work, therefore, simulations with PBC were made only for CASE IV, to generate some data corresponding to different but uncontrolled solid-flow rates. In CASE VI, coarse particles ($d_p = 2.05$ mm) with much larger density ($\rho_p = 2{,}500$ kg/m^3) are used, and, thus, only the stratified flow regime is observed even at high-gas velocities ($U_g = 23.0 - 35.0$ m/s). The pressure drops in CASE IV and CASE VI are also plotted in Figure 18. As can be seen from the figure, CASE IV has a high-pressure drop due to the presence of slugs in the pipe although the velocity considered is very low, while the pressure drops in CASE VI is relatively low as the flow patterns involved are in the stratified flow regime. These are consistent with the results in the first three cases, and qualitatively agree with our general observations of horizontal pneumatic conveying.[3,11,14]

Figure 17 shows the results in the new phase diagrams for all the cases considered. It is of great interest to note that in the new diagram all the simulation data collapse in one curve, although the data in Figure 18 are very scattered particularly at the relatively low-gas velocities. Note that the data in Figure 17b at a particle scale are slightly more scattered than those in Figure 17a at the pipe scale. This may be attributed to the chaotic flow behavior of particles and the resulting particle–particle collisions. Nonetheless, these results indicate the generality of the new phase diagram.

Compared to the pressure drop-gas velocity phase diagram, the new phase diagram as shown in Figure 17 not only has a profile independent of the conditions considered, but also can better represent the underlying fundamentals. For example, it highlights an important characteristic of a dilute-phase flow that the particle–particle and particle-wall forces are small, if not negligible, compared to those in a dense-phase flow. Here, the so-called dilute-phase flow is a flow where $\prod_1$ almost keeps constant and small, corresponding to the dispersed flow regime and the stratified flow regime, and the dense-phase flow is a flow where $\prod_2$ increases with the increase of $\prod_1$, corresponding to the slug-flow regime and the transition flow regime. The concepts are similar to those used in the pressure drop-gas velocity phase diagram. However, physically, they are different. In the old phase diagram, the division between the dilute- and dense-phase flows is based on the decrease and increase of pressure drop, as shown in Figure 2. It is case-dependent, as shown in Figure 18. This problem can be overcome in the new phase diagram as noted earlier. This is because the new diagram is based directly on the forces governing the behaviors of particles and, hence, is fundamentally more reliable. On the other hand, visual observations give more flow regimes. Some of these flow regimes (stratified flow and transition flow) cannot be recognized in this phase diagram. While the need for their full reorganization is questionable, it is certainly useful to better understand the transition flow regime that can be identified in the pressure drop-gas velocity diagram. This will be investigated further in our future research.

Conclusions

A 3-D CFD-DEM model has been used to study the flow regimes in horizontal pneumatic conveying. The results from this work can be summarized as follows:

1. This model can satisfactorily capture the key flow behaviors observed, such as particle flow pattern and gas pressure characteristics. In particular, it can reproduce the transition from slug-flow regime, to transition flow, to stratified flow regime, and finally to dispersed flow regime with the increase of gas velocity for given conveying conditions.

2. The mechanisms underlying the relationship between pressure drop and gas velocity have been analyzed. It is shown that the pressure drop in the slug-flow regime and the transition flow is controlled by the fluid-drag force and pressure gradient force. However, the pressure gradient force is close to zero in the stratified flow regime and the dispersed flow regime, and the pressure drop is mainly dependent on the gas-wall friction force and fluid-drag force.

3. The forces governing the flow of particles have been analyzed at the pipe and particle scales, resulting in the establishment of a new phase diagram to distinguish the dense- and dilute-phase flows. In the diagram, the particle–particle and/or particle-wall force increases with the increase of the particle-fluid force in the slug-flow regime and the transition flow regime, but is small, if not negligible, in the stratified flow regime and the dispersed flow regime. There is evidence showing the changes of material properties, flow condition or pipe geometry will not affect the trends established in this diagram.

Acknowledgments

The authors are grateful to the Australia Research Council (ARC) for the financial support of this work, the Australian Center for Advanced Computing and Communications (AC3) for the use of its computational facilities.

Notation

d = particle diameter, m
D = diameter of pipe
E = Young's modulus, Pa
$\mathbf{f}$ = particle scale forces, N
$\mathbf{F}$ = volumetric force, $\mathrm{N{\cdot}m^{-3}}$
$\mathbf{g}$ = gravitational acceleration, $\mathrm{m{\cdot}s^{-2}}$
I = moment of inertia of particle, $\mathrm{kg{\cdot}m^2}$
k = turbulent kinetic energy
k_i = number of particles in contact with particle i
L = length of pipe, m
$\mathbf{T}$ = torque, N·m
m = mass of particle, kg
P = pressure, Pa
$\Delta\mathbf{r}$ = vector from cell center to particle center position, m
$\mathbf{R}$ = vector from the mass center of the particle to the contact point, m
t = time, s
$\mathbf{v}$ = particle translational velocity, $\mathrm{m{\cdot}s^{-1}}$
V = volume, $\mathrm{m^3}$
$\mathbf{u}$ = gas velocity, $\mathrm{m{\cdot}s^{-1}}$
u_i = the component of the velocity vector $\mathbf{u}$
U = superficial velocity, $\mathrm{m{\cdot}s^{-1}}$
w = mass flow rate, $\mathrm{kg{\cdot}s^{-1}}$
x_i = Cartesian coordinate

Greek

$\boldsymbol{\delta}_t$ = vector of the accumulated tangential displacement between particles i and j
ε = dissipation of turbulent kinetic energy
ε_f = porosity
γ = damping coefficient
η = gas viscosity, $\mathrm{kg{\cdot}m^{-1}{\cdot}s^{-1}}$
ρ = density, $\mathrm{kg{\cdot}m^{-3}}$
$\boldsymbol{\omega}$ = particle angular velocity, $\mathrm{s^{-1}}$
$\hat{\boldsymbol{\omega}}$ = unit vector defined by $\hat{\boldsymbol{\omega}} = \boldsymbol{\omega}/|\boldsymbol{\omega}|$
μ = friction coefficient
$\boldsymbol{\tau}$ = fluid viscous stress tensor, $\mathrm{kg{\cdot}m^{-1}{\cdot}s^{-2}}$

Subscripts

c = contact
cell = computational cell
d = damping
drag = fluid-drag force
f = fluid
i = particle i
ij = between particles i and j
j = particle j
n = normal component
p = particle
p-f = particle-fluid
pgf = pressure gradient force
r = rolling friction
s = sliding
section = pipe section
t = tangential component

Literature Cited

1. Mills D. *Pneumatic Conveying Design Guide*. London: Butterworths; 2004.
2. Jama GA, Klinzing GE, Rizk F. An investigation of the prevailing flow patterns and pressure fluctuation near the pressure minimum and unstable conveying zone of pneumatic transport systems. *Powder Technol*. 2000;112:87–93.
3. Lecreps I, Sommer K. Horizontal dense-phase pneumatic conveying of granular material. *Bulk Solids Powder - Sci Technol*. 2007;2:95–105.
4. Jones MG, Williams KC. Predicting the mode of flow in pneumatic conveying systems-a review. *Particuology*. 2008;6:289–300.
5. Sanchez L, Vasquez N, Klinzing GE, Dhodapkar S. Characterization of bulk solids to assess dense phase pneumatic conveying. *Powder Technol*. 2003;138:93–117.
6. Pahk JB, Klinzing GE. Assessing flow regimes from pressure fluctuations in pneumatic conveying of polymer pellets. *Part Sci Technol*. 2008;26:247–256.
7. Li J, Pandiella SS, Webb C, McGlinchey D, Cowell A, Xiang J, Knight L, Pugh J. An experimental technique for the analysis of slug flows in pneumatic pipelines using pressure measurements. *Part Sci Technol*. 2002;20:283–303.
8. Dhodapkar SV, Klinzing GE. Pressure-fluctuations in pneumatic conveying systems. *Powder Technol*. 1993;74:179–195.
9. Matsumoto S, Harakawa H. Statistical-analysis of the transition of the flow pattern in vertical pneumatic conveying. *Int J Multiphase Flow*. 1987;13:123–129.
10. Tsuji Y, Morikawa Y. Flow pattern and pressure fluctuation in air-solid two-phase flow in a pipe at low air velocities. *Int J Multiphase Flow*. 1982;8:329–341.
11. Wypych PW, Yi JL. Minimum transport boundary for horizontal dense-phase pneumatic conveying of granular materials. *Powder Technol*. 2003;129:111–121.
12. Pan R. Material properties and flow modes in pneumatic conveying. *Powder Technol*. 1999;104:157–163.
13. Jama GA, Klinzing GE, Rizk F. Analysis of unstable behavior of pneumatic conveying systems. *Part Sci Technol*. 1999;17:43–68.
14. Molerus O. Overview: Pneumatic transport of solids. *Powder Technol*. 1996;88:309–321.
15. Sanchez L, Vasquez NA, Klinzing GE, Dhodapkar S. Evaluation of models and correlations for pressure drop estimation in dense phase pneumatic conveying and an experimental analysis. *Powder Technol*. 2005;153:142–147.
16. Mallick SS, Wypych PW. Minimum transport boundaries for pneumatic conveying of powders. *Powder Technol*. 2009;194:181–186.
17. Narimatsu CP, Ferreira MC. Vertical pneumatic conveying in dilute and dense-phase flows: Experimental study of the influence of particle density and diameter on fluid dynamic behavior. *Braz J Chem Eng*. 2001;18:221–232.
18. Bi HT, Grace JR, Zhu JX. Types of choking in vertical pneumatic systems. *Int J Multiphase Flow*. 1993;19:1077–1092.

19. Dyakowski T, Jeanmeure LFC, Jaworski AJ. Applications of electrical tomography for gas-solids and liquid-solids flows - a review. *Powder Technol*. 2000;112:174–192.
20. Fokeer S, Kingman S, Lowndes I, Reynolds A. Characterisation of the cross sectional particle concentration distribution in horizontal dilute flow conveying - a review. *Chem Eng Process*. 2004;43:677–691.
21. Takei M, Ochi M, Saito Y. Image extraction of particle concentration at the plug front using 3d wavelets and comparison with LDV. *Powder Technol*. 2004;142:70–78.
22. Zhu KW, Rao SM, Wang CH, Sundaresan S. Electrical capacitance tomography measurements on vertical and inclined pneumatic conveying of granular solids. *Chem Eng Sci*. 2003;58:4225–4245.
23. Rao SM, Zhu KW, Wang CH, Sundaresan S. Electrical capacitance tomography measurements on the pneumatic conveying of solids. *Ind Eng Chem Res*. 2001;40:4216–4226.
24. Jaworski AJ, Dyakowski T. Application of electrical capacitance tomography for measurement of gas-solids flow characteristics in a pneumatic conveying system. *Measure Sci Technol*. 2001;12:1109–1119.
25. Lecreps I, Sommer K, Wolz K. Stress states and porosity within horizontal slug by dense-phase pneumatic conveying. *Part Sci Technol*. 2009;27:297–313.
26. Niederreiter G, Sommer K. Modeling and experimental validation of pressure drop for pneumatic plug conveying. *Granular Matter*. 2004;6:179–183.
27. Krull T, Jones MG, Keys S. Stress-field modeling and pressure drop prediction for slug-flow pneumatic conveying in an aerated radial stress chamber. *Part Sci Technol*. 2004;22:129–138.
28. Vasquez N, Sanchez L, Klinzing GE, Dhodapkar S. Friction measurement in dense phase plug flow analysis. *Powder Technol*. 2003;137:167–183.
29. Van der Hoef MA, Annaland MV, Deen NG, Kuipers JAM. Numerical simulation of dense gas-solid fluidized beds: A multiscale modeling strategy. *Annual Rev Fluid Mechanics*. 2008;40: 47–70.
30. Zhu HP, Zhou ZY, Yang RY, Yu AB. Discrete particle simulation of particulate systems: Theoretical developments. *Chem Eng Sci*. 2007;62:3378–3396.
31. Tsuji Y. Multi-scale modeling of dense phase gas-particle flow. *Chem Eng Sci*. 2007;62:3410–3418.
32. Enwald H, Peirano E, Almstedt AE. Eulerian two-phase flow theory applied to fluidization. *Int J Multiphase Flow*. 1996;22:21–66.
33. Nakamura K, Capes CE. Vertical pneumatic conveying - theoretical study of uniform and annular particle flow models. *Can J Chem Eng*. 1973;51:39–46.
34. Henthorn KH, Park K, Curtis JS. Measurement and prediction of pressure drop in pneumatic conveying: Effect of particle characteristics, mass loading, and Reynolds number. *Ind Eng Chem Res*. 2005;44:5090–5098.
35. Hadinoto K, Jones EN, Yurteri C, Curtis JS. Reynolds number dependence of gas-phase turbulence in gas-particle flows. *Int J Multiphase Flow*. 2005;31:416–434.
36. Lee LY, Quek TY, Deng RS, Ray MB, Wang CH. Pneumatic transport of granular materials through a 90 degrees bend. *Chem Eng Sci*. 2004;59:4637–4651.
37. Hadinoto K, Curtis JS. Effect of interstitial fluid on particle-particle interactions in kinetic theory approach of dilute turbulent fluid-particle flow. *Ind Eng Chem Res*. 2004;43:3604–3615.
38. Curtis JS, van Wachem B. Modeling particle-laden flows: A research outlook. *AIChE J*. 2004;50:2638–2645.
39. Zhu KW, Wong CK, Rao SM, Wang CH. Pneumatic conveying of granular solids in horizontal and inclined pipes. *AIChE J*. 2004;50:1729–1745.
40. Levy A, Mooney T, Marjanovic P, Mason DJ. A comparison of analytical and numerical models with experimental data for gas-solid flow through a straight pipe at different inclinations. *Powder Technol*. 1997;93:253–260.
41. Pu WH, Zhao CS, Xiong YQ, Liang C, Chen XP, Lu P, Fan CL. Three-dimensional numerical simulation of dense pneumatic conveying of pulverized coal in a vertical pipe at high pressure. *Chem Eng Technol*. 2008;31:215–223.
42. Xu BH, Yu AB. Numerical simulation of the gas-solid flow in a fluidized bed by combining discrete particle method with computational fluid dynamics. *Chem Eng Sci*. 1997;52:2785–2809.
43. Tsuji Y, Tanaka T, Ishida T. Lagrangian numerical-simulation of plug flow of cohesionless particles in a horizontal pipe. *Powder Technol*. 1992;71:239–250.
44. Huber N, Sommerfeld M. Modelling and numerical calculation of dilute-phase pneumatic conveying in pipe systems. *Powder Technol*. 1998;99:90–101.
45. Yilmaz A, Levy EK. Formation and dispersion of ropes in pneumatic conveying. *Powder Technol*. 2001;114:168–185.
46. Quek TY, Wang CH, Ray MB. Dilute gas-solid flows in horizontal and vertical bends. *Ind Eng Chem Res*. 2005;44:2301–2315.
47. Kuan B, Rea N, Schwarz MP. Application of CFD in the design of a grit collection system for the coal-fired power generation industry. *Powder Technol*. 2007;179:65–72.
48. Zhu HP, Zhou ZY, Yang RY, Yu AB. Discrete particle simulation of particulate systems: A review of mayor applications and findings. *Chem Eng Sci*. 2008;63:5728–5770.
49. Kuang SB, Yu AB, Zou ZS. Computational study of flow regimes in vertical pneumatic conveying. *Ind Eng Chem Res*. 2009;48:6846–6858.
50. Lim EWC, Wang CH, Yu AB. Discrete element simulation for pneumatic conveying of granular material. *AIChE J*. 2006;52:496–509.
51. Fraige FY, Langston PA. Horizontal pneumatic conveying: A 3d distinct element model. *Granular Matter*. 2006;8:67–80.
52. Strauβ M, McNamara S, Herrmann HJ. Plug conveying in a horizontal tube. *Granular Matter*. 2007;9:35–48.
53. Strauβ M, McNamara S, Herrmann HJ, Niederreiter G, Sommer K. Plug conveying in a vertical tube. *Powder Technol*. 2006;162: 16–26.
54. Chu KW, Yu AB. Numerical simulation of the gas-solid flow in three-dimensional pneumatic conveying bends. *Ind Eng Chem Res*. 2008;47:7058–7071.
55. Kuang SB, Yu AB, Zou ZS. A new point-locating algorithm under three-dimensional hybrid meshes. *Int J Multiphase Flow*. 2008; 34:1023–1030.
56. Di Felice R. The voidage function for fluid particle interaction systems. *Int J Multiphase Flow*. 1994;20:153–159.
57. Zhou ZY, Zhu HP, Yu AB, Wright B, Zulli P. Discrete particle simulation of gas-solid flow in a blast furnace. *Comput Chem Eng*. 2008;32:1760–1772.
58. Kuang SB, Chu KW, Yu AB, Zou ZS, Feng YQ. Computational investigation of horizontal slug flow in pneumatic conveying. *Ind Eng Chem Res*. 2008;47:470–480.
59. Chu KW, Wang B, Yu AB, Vince A. CFD-DEM modeling of multiphase flow in dense medium cyclones. *Powder Technol*. 2009; 193:235–247.
60. Zhou YC, Wright BD, Yang RY, Xu BH, Yu AB. Rolling friction in the dynamic simulation of sandpile formation. *Physica A*. 1999; 269:536–553.
61. Pita JA, Sundaresan S. Gas-solid flow in vertical tubes. *AIChE J*. 1991;37:1009–1018.
62. Pita JA, Sundaresan S. Developing flow of a gas-particle mixture in a vertical riser. *AIChE J*. 1993;39:541–552.
63. Louge MY, Mastorakos E, Jenkins JT. The role of particle collisions in pneumatic transport. *J Fluid Mech*. 1991;231:345–359.
64. Gosman AD, Ioannides E. Aspects of computer-simulation of liquid-fueled combustors. *J Energy*. 1983;7:482–490.
65. Cundall PA, Strack ODL. Discrete numerical-model for granular assemblies. *Geotechnique*. 1979;29:47–65.
66. Partankar SV. *Numerical Heat Transfer and Fluid Flow*. Washington, DC: Hemisphere Publishing Co; 1980.
67. Ferziger J, Peric M. *Computational Methods for Fluid Dynamics*. 3rd ed. New York: Springer; 2002.
68. Li J, Mason DJ. A computational investigation of transient heat transfer in pneumatic transport of granular particles. *Powder Technol*. 2000;112:273–282.
69. Kawaguchi T, Tanaka T, Tsuji Y. Numerical analysis of density wave in dense gas-solid flows in a vertical pipe. *Prog Theoretical Phys Suppl*. 2000:696–701.

70. Li J, Webb C, Pandiella SS, Campbell GM, Dyakowski T, Cowell A, McGlinchey D. Solids deposition in low-velocity slug flow pneumatic conveying. *Chem Eng Process*. 2005;44:167–173.
71. Mi B, Wypch PW. Pressure-drop prediction in low-velocity pneumatic conveying. *Powder Technol*. 1994;81:125–137.
72. Borzone LA, Klinzing GE. Dense-phase transport-vertical plug flow. *Powder Technol*. 1987;53:273–283.
73. Tomita Y, Jotaki T, Hayashi H. Wave-like motion of particulate slugs in a horizontal pneumatic pipeline. *Int J Multiphase Flow*. 1981;7:151–166.
74. Ratnayake C, Datta BK, Melaaen MC. A unified scaling-up technique for pneumatic conveying systems. *Part Sci Technol*. 2007;25:289–302.
75. Nowak M. Wall shear stress measurement in a turbulent pipe flow using ultrasound doppler velocimetry. *Exp Fluids*. 2002;33:249–255.

Manuscript received Apr. 14, 2010, and revision received Oct. 14, 2010.